Journal of Drug Delivery Science and Technology 126 (2026) 108800

Contents lists available at ScienceDirect

Journal of Drug Delivery Science and Technology

journal homepage: www.elsevier.com/locate/jddst

Sodium alginate/polyvinylpyrrolidone-gated ZIF-8 nanocarriers for pH-selective sustained docetaxel delivery

Sepideh Asadi [a], Iman Barzgar [b,1], Arman Barzgar [b,1], Hanieh Eftekhari [c], Leila Jamei [d], Fatemeh Hasibi [e], Yavuz Nuri Ertas [f,*]

[a] Department of Nanobiotechnology and Biomimetics, School of Life Science Engineering, College of Interdisciplinary Science and Technology, University of Tehran, Tehran, 14399-57131, Iran
[b] Department of Biomedical Engineering, Sadjad University, Mashhad, 91881-48848, Iran
[c] Department of Biomedical Engineering, Science and Research Branch, Islamic Azad University, Tehran, 14778-93855, Iran
[d] Department of Chemistry, Isfahan University of Technology, Isfahan, 84156-83111, Iran
[e] Rajiv Gandhi University of Health Sciences, Bengaluru, 560041, India
[f] Department of Biomedical Engineering, Erciyes University, Kayseri, 38039, Türkiye

ARTICLE INFO

Keywords:
Docetaxel
ZIF-8
Sodium alginate
Polyvinylpyrrolidone
pH-dependent release
Breast cancer

ABSTRACT

Docetaxel (DOC) is a cornerstone in breast cancer chemotherapy, yet its clinical utility is constrained by poor aqueous solubility and systemic toxicity. We report a hybrid nanocarrier that couples an acid-labile zeolitic imidazolate framework-8 (ZIF-8) reservoir with a biocompatible, diffusion-modulating polymer gate composed of sodium alginate (SA)/polyvinylpyrrolidone (PVP) to enable pH-selective, sustained release. The DOC@ZIF-8/SA/PVP composite was synthesized and characterized. XRD confirmed preserved ZIF-8 crystallinity, and FTIR spectra retained characteristic imidazolate bands. Particles showed a unimodal hydrodynamic distribution (hydrodynamic diameter = 184 nm) with a moderately negative zeta potential of −27.6 mV. Nitrogen sorption analysis of pristine ZIF-8 revealed a type I isotherm with a BET surface area of 1171 m^2/g and a micropore volume of 0.339 cm^3/g, confirming the highly porous nature of the MOF core used for drug loading. *In vitro*, the coated system exhibited pH-selective sustained release, reaching 95% at pH 5.5 (96–120 h) versus 59% at pH 7.4 (120 h), whereas bare DOC@ZIF-8 released ≤25% (pH 5.5) and 14% (pH 7.4) over the same window. Release kinetics followed the Korsmeyer-Peppas model, indicating a predominantly Fickian diffusion mechanism. In MCF-7 breast cancer cells and NIH3T3 mouse embryonic fibroblasts, DOC@ZIF-8/SA/PVP showed a therapeutic response window between cancer and normal cells, with lower apparent potency than free DOC in MCF-7 cells and reduced toxicity toward NIH3T3 fibroblasts. These findings indicate that the polymer-gated ZIF-8 system improves controlled, pH-selective DOC delivery while reducing normal-cell toxicity, rather than increasing DOC's intrinsic potency. The integration of an MOF reservoir with a polymer gate enables pH-responsive, sustained release of DOC, thereby improving controlled delivery and maintaining biocompatibility *in vitro*. Overall, the MOF reservoir/polymer gate formulation provides a promising platform for pH-selective DOC delivery and warrants further *in vivo* evaluation of pharmacokinetics, biodistribution, antitumor efficacy, and safety.

1. Introduction

Breast cancer remains the most commonly diagnosed cancer among women worldwide and is a leading cause of cancer-related mortality [1]. Although major advances have been made in human epidermal growth factor receptor 2 (HER2)-targeted therapy [2], radiotherapy [3], endocrine therapy [4], and surgery [5], cytotoxic chemotherapy remains central to the treatment of several subtypes, particularly triple-negative breast cancer, for which taxanes are standard first-line agents [6]. Despite the widespread use of docetaxel (DOC), a microtubule-stabilizing taxane used in early-stage and metastatic breast cancer, systemic toxicity and off-target exposure continue to limit its therapeutic index [7]. Commercial DOC formulations commonly require polysorbate 80 and ethanol to overcome the drug's low aqueous

* Corresponding author. Department of Biomedical Engineering, Erciyes University, Kayseri, 38039, Türkiye.
E-mail address: yavuznuri@gmail.com (Y.N. Ertas).
[1] These authors contributed equally to the work.

https://doi.org/10.1016/j.jddst.2026.108800
Received 25 December 2025; Received in revised form 5 August 2026; Accepted 6 August 2026
Available online 7 August 2026
1773-2247/© 2026 Elsevier B.V. All rights are reserved, including those for text and data mining, AI training, and similar technologies.

solubility (typically 6–7 μg/mL), but these excipients contribute to hypersensitivity reactions and other dose-limiting toxicities. In addition, DOC is susceptible to multidrug resistance mechanisms, including P-glycoprotein-mediated efflux, which can reduce intracellular drug accumulation and therapeutic efficacy [8].

Nanocarriers can improve spatiotemporal delivery by increasing solubility, prolonging circulation, and enabling microenvironment-responsive release in the TME. Because the EPR effect is heterogeneous in human tumors, pH-selective designs are increasingly useful for achieving reliable tumor-selective delivery [9–11]. Zeolitic imidazolate framework-8 (ZIF-8; Zn(2-methylimidazolate)$_2$) is an archetypal metal-organic framework with considerable potential for drug delivery because of its high porosity and surface area, facile synthesis in aqueous or alcoholic media, and acid-labile Zn–imidazolate coordination, which promotes framework disassembly under acidic endosomal and lysosomal conditions and supports enhanced drug release in acidic tumor-associated environments. At the same time, unmodified MOF particles can aggregate and may interact nonspecifically with proteins; polymer hybridization helps mitigate these issues. Sodium alginate (SA) and polyvinylpyrrolidone (PVP) are two pharmaceutically established, biocompatible polymers with complementary functions: SA, an anionic polysaccharide, affords aqueous stability and pH-responsive swelling, while PVP provides steric stabilization and dispersibility and can guide crystal growth of inorganic phases. Prior SA/PVP hybrids have improved drug loading, colloidal stability, and pH-modulated release in the delivery of cytotoxic payloads, motivating their use as an outer matrix or shell to regulate MOF behavior in biological media [12,13]. Indeed, SA/PVP nanocomposites have been reported to exhibit high encapsulation efficiencies and pH-dependent release profiles while maintaining cytocompatibility in normal fibroblasts. For instance, SA/PVP/γ-Al_2O_3 nanocarriers loaded with curcumin achieved an encapsulation efficiency of 92.4 ± 1.8%. The curcumin-loaded SA/PVP/γ-Al_2O_3 nanocarriers demonstrated pH-selective release; cell viability remained consistently >90% in L929 fibroblasts, while HCT116 colon cancer cell viability decreased to 40% [14]. Similarly, clay-alginate nanocomposites loaded with 5-fluorouracil exhibited a zeta potential of −39.8 mV, an encapsulation efficiency of 94.6%, and enhanced release under acidic conditions that mimic the TME [15].

For DOC delivery, ZIF-8 offers several complementary advantages. Its high surface area, intrinsic microporosity, and accessible surface chemistry provide a favorable environment for DOC association through hydrophobic and π–π interactions. In addition, the acid-labile ZIF-8 framework undergoes accelerated destabilization under acidic endosomal and lysosomal conditions, thereby facilitating drug release following cellular internalization. The incorporation of an SA/PVP polymer gate further improves aqueous compatibility and interfacial stability, moderates premature drug release at physiological pH, and supports the hemocompatibility of the resulting formulation. Nevertheless, two translational realities motivate our hybrid approach. First, the EPR effect in patients is variable; thus, placing greater emphasis on microenvironment-responsive release can improve robustness across tumors with disparate vasculature [16]. Second, eliminating polysorbate 80/ethanol from the formulation could reduce excipient-related toxicities while preserving or enhancing antitumor activity by increasing intratumoral exposure. SA/PVP shells around ZIF-8 can provide aqueous dispersibility, control interfacial interactions with serum proteins, and reduce premature DOC leakage without introducing new surfactant liabilities [17].

In this study, to address DOC's solubility and off-target exposure while retaining high loading capacity, we developed a pH-selective DOC delivery platform by integrating an acid-labile ZIF-8 reservoir with an SA/PVP polymer gate. The objective was to synthesize DOC@ZIF-8/SA/PVP nanocarriers, characterize their physicochemical properties, evaluate DOC loading and pH-dependent release behavior, analyze release kinetics, and assess their *in vitro* anticancer activity, cytocompatibility, and hemocompatibility. This design was intended to combine the high loading capacity and acid-responsive behavior of ZIF-8 with the stabilizing and diffusion-modulating functions of SA/PVP.

2. Materials and methods

2.1. Materials

The following substances were purchased from Sigma-Aldrich: sodium alginate (SA), polyvinylpyrrolidone (PVP), zinc nitrate hexahydrate ($Zn(NO_3)_2{\cdot}6H_2O$), and 2-methylimidazole (Hmim) for the synthesis of ZIF-8, as well as docetaxel (DOC, ≥99% purity) as the model anticancer drug. Analytical-grade methanol, ethanol, and phosphate-buffered saline (PBS) were obtained from Merck (Germany). All reagents were used as received without further purification. Deionized double-distilled water was used throughout the experiments. Human breast cancer cells (MCF-7) and mouse embryonic fibroblast cells (NIH3T3) were obtained from the Pasteur Institute of Iran. Dulbecco's modified Eagle medium (DMEM), fetal bovine serum (FBS), penicillin-streptomycin (P/S), and trypsin-EDTA were supplied by Gibco (Thermo Fisher Scientific, USA). The MTT reagent for cytotoxicity assays was purchased from Sigma-Aldrich. Cell cultures were maintained at 37 °C in a humidified atmosphere containing 5% CO_2.

2.2. Synthesis of ZIF-8/SA/PVP nanocarriers

The core of the ZIF-8/SA/PVP nanocarriers was prepared by rapid aqueous precipitation of ZIF-8. In brief, 2.94 g of 2-methylimidazole (Hmim) was dissolved in 40 mL of deionized water. Separately, 0.80 g of $Zn(NO_3)_2{\cdot}6H_2O$ was dissolved in 20 mL of deionized water. The zinc nitrate solution was added to the Hmim solution, and the mixture was homogenized (10,000 rpm, 10 min) to obtain ZIF-8 nanoparticles. The nanoparticles were collected by centrifugation (10,000 rpm, 10 min), washed three times with ethanol and deionized water, and dried at 60 °C overnight. For the polymer coating, sodium alginate (SA, 0.70 g) was dissolved in 35 mL of deionized water under continuous stirring at room temperature to obtain a clear 2% (w/v) solution.

The reagent concentrations used were 0.90 M Hmim (2.94 g in 40 mL) and 0.135 M $Zn(NO_3)_2{\cdot}6H_2O$ (0.80 g in 20 mL), corresponding to an Hmim: Zn^{2+} molar ratio of 13.3:1. Next, 0.35 g of PVP was added to the SA solution to obtain an SA:PVP mass ratio of 2:1 (total polymer = 3% w/v). The mixture was sonicated for 10 min to ensure complete homogenization. The ZIF-8 nanoparticles (35 mg) were then added to the SA/PVP solution, and the mixture was stirred until a homogeneous suspension was obtained. The coated ZIF-8/SA/PVP nanocarriers were collected by centrifugation at 10,000 rpm for 10 min, washed with deionized water and ethanol, and dried at 60 °C before drug loading.

2.3. Characterization of DOC@ZIF-8/SA/PVP nanocarriers

2.3.1. FTIR spectroscopy

FTIR spectra were recorded on a benchtop FTIR spectrometer in attenuated total reflectance (ATR) mode over the range of 4000–500 cm^{-1}, with a resolution of 4 cm^{-1} and 32 scans). Spectra of ZIF-8, SA, PVP, physical mixtures, ZIF-8/SA, ZIF-8/SA/PVP, DOC, and DOC@ZIF-8/SA/PVP were collected and baseline-corrected before analysis.

2.3.2. XRD analysis

X-ray diffraction analysis was performed to investigate the crystalline structures of pristine ZIF-8, ZIF-8/SA, and ZIF-8/SA/PVP. XRD patterns were recorded using a Bruker D8 Advance (Bruker AXS, Germany) diffractometer equipped with Cu-Kα radiation (λ = 1.5406 Å), operated at 40 kV and 30 mA. Data were collected over a 2θ range of 5°–80° at a scan rate of 2° min^{-1}.

2.3.3. DLS and zeta potential analysis

Hydrodynamic diameter and polydispersity index (PDI) were measured by dynamic light scattering (DLS) using a Zetasizer Nano ZS (Malvern) at 25 ± 0.1 °C using disposable cuvettes. Zeta potential was determined by electrophoretic light scattering in folded capillary cells at 25 °C. All measurements were performed in triplicate on freshly sonicated dispersions.

2.3.4. FE-SEM analysis

Morphology was examined by field-emission scanning electron microscopy (FE-SEM) using a MIRA3 instrument (TESCAN, Czech Republic). Samples were sputter-coated with a thin gold layer. Elemental maps (C, N, O, Na, Zn) were acquired by energy-dispersive X-ray spectroscopy (EDS) with the FE-SEM operated at an accelerating voltage of 15 kV.

2.3.5. BET surface area and pore structure analysis

Specific surface area and pore structure of ZIF-8 were determined by N_2 adsorption-desorption isotherms at 77 K using a BET surface area analyzer (Micromeritics ASAP 2020, Micromeritics Instrument, USA). Samples were vacuum-degassed prior to measurement, and BET and t-plot analyses were performed to determine surface area, pore volumes, and pore-size distributions in accordance with IUPAC guidelines. The BET surface area was determined from the adsorption branch using a relative-pressure range of $P/P_0 = 0.01996–0.06031$. The selected fitting range provided a positive BET constant and high linearity in the BET plot. Total pore volume was estimated from the adsorbed volume near $P/P_0 \approx 0.99$, while micropore volume was obtained using t-plot analysis.

2.4. Drug loading and encapsulation efficiency

DOC was loaded into the preformed ZIF-8/SA/PVP nanocarriers via post-synthesis adsorption and diffusion rather than in situ encapsulation during ZIF-8 formation [18,19]. Briefly, 10 mg of pre-synthesized ZIF-8/SA/PVP nanocarriers were dispersed in 10 mL of an ethanol–water mixture (1:1 v/v) containing 2 mg of DOC. The suspension was magnetically stirred at 300 rpm for 24 h at room temperature in the dark to facilitate diffusion of the drug into the porous ZIF-8 core and interaction of the drug with the SA/PVP polymer shell. After incubation, the mixture was centrifuged at 10,000 rpm for 10 min, and the supernatant was collected for analysis of unbound drug. The drug-loaded nanocarriers (DOC@ZIF-8/SA/PVP) were washed once with 2 mL of ethanol–water (1:1 v/v) to remove loosely bound DOC and then dried under vacuum at 40 °C. The amount of DOC loaded into the nanocarriers was quantified by UV–Vis spectrophotometry at $\lambda_{max} = 229$ nm, using a standard calibration curve prepared in a 1:1 (v/v) ethanol–water mixture. The drug loading content (DLC) and encapsulation efficiency (EE) were calculated according to the following equations:

$$\text{DLC}\ (\%) = \left(\frac{W_{\text{initial DOC}} - W_{\text{free DOC}}}{W_{\text{drug–loaded nanocarriers}}}\right) \text{x}\ 100 \qquad \text{Equation (1)}$$

$$\text{EE}\ (\%) = \left(\frac{W_{\text{initial DOC}} - W_{\text{free DOC}}}{W_{\text{initial DOC}}}\right) \text{x}\ 100 \qquad \text{Equation (2)}$$

where $W_{\text{initial DOC}}$ is the initial amount of docetaxel used in the loading process, $W_{\text{free DOC}}$ is the amount of unloaded (free) docetaxel remaining in the supernatant after loading, and $W_{\text{drug-loaded nanocarriers}}$ is the total mass of the drug-loaded nanocarrier formulation. All experiments were conducted in triplicate, and results are reported as mean ± standard deviation (SD).

2.5. Investigation of in vitro drug release

The *in vitro* drug-release behavior of DOC@ZIF-8/SA/PVP nanocarriers was evaluated using a protocol designed to ensure sink conditions and to accommodate DOC's poor aqueous solubility [20]. Dialysis was performed using dialysis bags with a molecular weight cutoff of 12–14 kDa. A nanocarrier suspension at 5 mg/mL was loaded into dialysis bags, which were then immersed in 100 mL of release medium under constant stirring at 100 rpm in a shaking incubator (IKA KS 4000i, Germany) maintained at 37 °C. To maintain sink conditions, the release medium was supplemented with 0.5% (w/v) Tween 80, a nonionic surfactant known to enhance the solubility of hydrophobic drugs such as DOC. Tween 80 was used exclusively to maintain sink conditions for *in vitro* testing and is not part of the final drug formulation. The release study was conducted at two pH values: pH 7.4 to represent physiological conditions and pH 5.5 to represent acidic endosomal/lysosomal conditions. At predetermined time points, 2 mL aliquots were withdrawn and replaced with an equal volume of fresh, pre-warmed buffer containing Tween 80 to preserve sink conditions throughout the experiment. The concentration of DOC released into the medium was determined by UV–Vis spectrophotometry at 229 nm, using a calibration curve prepared in the same release medium.

2.6. In vitro cytotoxicity assessment

The cytotoxicity of DOC@ZIF-8/SA/PVP nanocarriers was evaluated using the MTT assay in MCF-7 human breast cancer cells and NIH3T3 mouse embryonic fibroblasts [21]. Cells were cultured in Dulbecco's modified Eagle medium (DMEM) supplemented with 10% fetal bovine serum (FBS) and 1% penicillin-streptomycin. They were maintained in a humidified atmosphere at 37 °C with 5% CO_2 (Heracell 150i, Thermo Fisher Scientific). For the assay, cells were seeded at 1×10^4 cells/well in 96-well plates and allowed to attach for 24 h. Subsequently, cells were treated with varying concentrations of DOC-loaded nanocarriers and incubated for 48 h. After treatment, 20 μL of MTT solution (5 mg/mL in PBS) was added to each well, and the plates were incubated for an additional 4 h to allow the formation of formazan crystals. The culture medium was then carefully removed, and the formazan crystals were dissolved in 150 μL of dimethyl sulfoxide (DMSO). Absorbance was measured at 570 nm using a microplate reader (SpectraMax M5, Molecular Devices, USA). Cell viability (%) was calculated by comparing the absorbance of treated cells to that of untreated controls. The cytotoxicity of free DOC, bare DOC@ZIF-8, DOC@ZIF-8/SA/PVP, unloaded ZIF-8/SA/PVP, pristine ZIF-8, SA, and PVP was evaluated under identical conditions for comparison.

2.7. Apoptotic gene expression analysis

MCF-7 cells were treated for 24 h with DOC@ZIF-8 or DOC@ZIF-8/SA/PVP at the respective IC_{50} concentration for each formulation. Total RNA was extracted from treated cells using an RNA extraction kit (Transgene Biotech), and cDNA was synthesized using a cDNA synthesis kit (Takara, Japan). The expression levels of *BAX, CDKN2A, CASP8,* and *CASP9* were analyzed by RT-qPCR, with *B2M* used as the reference gene. The primer sequences used for RT-qPCR are listed in Table S1. RT-qPCR was performed using SYBR® Green Master Mix (Bio-Rad, USA) on an iQ real-time PCR detection system. The cycling conditions consisted of an initial denaturation at 95 °C for 10 min, followed by 35 cycles at 95 °C for 15 s and 72 °C for 10 s. Relative gene expression levels were calculated from C_t values using the $2^{-\Delta\Delta Ct}$ method, with *B2M* used for normalization and the DOC@ZIF-8-treated group used as the calibrator. Agarose gel electrophoresis, when performed, was used only to confirm amplicon specificity and was not used for quantitative fold-change analysis.

2.8. Hemolysis assay

Commercially available human red blood cells (RBCs), supplied in anticoagulant-containing medium, were used for the hemolysis assay. Before use, the RBCs were washed three times with PBS by centrifugation at 1000 rpm for 10 min, as described in the literature [22].

DOC@ZIF-8/SA/PVP dispersions were prepared in saline at nominal concentrations of 400, 600, 800, 1000, and 1200 μg/mL. A 1.5 mL aliquot of each dispersion was mixed with 200 μL of washed RBC suspension and incubated at 37 °C for 1 h. The reported concentrations refer to the nominal sample concentrations of the samples before addition of the RBC suspension. Negative and positive controls were prepared by incubating 200 μL of RBC suspension with 1.5 mL of PBS and 1.5 mL of Triton X-100, respectively. After centrifugation at 1000 rpm for 10 min, the absorbance of the supernatant was measured at 540 nm using a PerkinElmer Lambda 25 UV–Vis spectrophotometer, and the hemolysis percentage was calculated using Equation (3):

$$\text{Hemolysis}\ (\%) = \left(\frac{(OD_s - OD_{nc})}{(OD_{pc} - OD_{nc})}\right) \text{x}\ 100 \qquad \text{Equation (3)}$$

where OD_s, OD_{nc}, and OD_{pc} are the optical densities of the sample, negative control, and positive control, respectively.

2.9. Statistical analysis

All experiments were performed in triplicate, and data were expressed as mean ± standard deviation (SD). Statistical analyses were carried out using OriginPro 2018. Differences between groups were evaluated using one-way analysis of variance (ANOVA) followed by Tukey's post hoc test for multiple comparisons. A value of $p < 0.05$ was considered statistically significant. Concentration–response curves were fitted by nonlinear regression using a four-parameter logistic model, and IC_{50} values were reported with their 95% confidence intervals.

3. Results and discussion

3.1. FTIR analysis results

Fig. 1a shows the FTIR spectra of the pure components, intermediates, and final composite nanocarriers. The typical imidazolate vibrations of pristine ZIF-8 include adsorbed O–H stretching at 3400–3460 cm^{-1}, C–H stretching at 2940 cm^{-1}, C=N stretching at 1580 cm^{-1}, ring stretching vibrations at 1420, 1145, and 995 cm^{-1}, and out-of-plane ring vibrations at 690–760 cm^{-1}; a weak Zn–N stretching band is also typically observed in the low-wavenumber region, further confirming the formation of the ZIF-8 framework. The sharp and well-defined imidazolate-related bands indicate preservation of the crystalline ZIF-8 structure. SA exhibited a broad O–H stretch at 3430 cm^{-1}, a C–H stretch at 2920 cm^{-1}, and asymmetric and symmetric carboxylate stretches at 1640 and 1410 cm^{-1}, respectively. The strong band at 1022 cm^{-1} is assigned to C–O–C and C–O stretching vibrations of the polysaccharide backbone, which is typical of alginate. Polyvinylpyrrolidone (PVP) showed a C–H stretching band at 2930 cm^{-1}, a sharp amide-I C=O at 1660–1670 cm^{-1}, a CH_2 bending band at 1430 cm^{-1}, and a C–N stretching near 1290 cm^{-1}, which are in line with the known PVP signatures. The original ZIF-8 peaks were retained in the spectrum of the ZIF-8/SA composite, but the O–H stretch broadened, and the intensities of the carboxylate and C–O/C–O–C bands increased. This overlay of features indicates the successful deposition of SA onto the ZIF-8 surface, with the MOF lattice remaining intact. In the case of ZIF-8/SA/PVP, the carbonyl band at approximately 1665 cm^{-1} increased in intensity and became slightly broader. The intensity of the C–N band at 1290 cm^{-1} also increased, indicating hydrogen bonding between the SA carboxylate groups and the PVP carbonyl groups. These changes in band position and intensity are consistent with hydrogen bonding between the SA carboxylates and PVP carbonyl groups and support successful polymer deposition on ZIF-8 without lattice collapse.

Pure DOC showed peaks at 3460 cm^{-1} (O–H stretching), 2925 cm^{-1} (C–H stretching), 1650 cm^{-1} (amide/aryl contributions), 1250 cm^{-1} (C–O/C–N stretching), and 1030 cm^{-1} (C–O stretching). The typical ZIF-8 and polymer bands were retained in the DOC@ZIF-8/SA/PVP spectrum after DOC loading into the ZIF-8/SA/PVP system. However, DOC-specific absorption bands at 1700 cm^{-1} (shifted C=O) and 1250 cm^{-1} were also visible, though slightly broadened. The absence of significant alterations in ZIF-8 framework peaks indicates that the MOF structure remained intact during the loading procedure. The retention of drug-specific peaks, together with broadening in the O–H and C=O regions, suggests the presence of hydrogen bonding and partial amorphous dispersion of DOC inside the polymer/MOF matrix.

3.2. XRD results

Canonical ZIF-8 with a sodalite topology exhibits characteristic low-angle reflections at approximately 7.3° (011), 10.4° (002), 12.7° (112), 14.7° (022), 16.4° (013), and 18.0° (222) under Cu-Kα radiation. These reflections were used as reference peaks for phase identification. The XRD pattern of pristine ZIF-8 reproduced the characteristic reflections as sharp and well-defined peaks, confirming the formation of a highly crystalline ZIF-8 phase (Fig. 1b) [23].

Following the sequential incorporation of SA and PVP, the characteristic peak positions of ZIF-8 remained unchanged, indicating preservation of the underlying crystalline framework. However, the relative intensities of the ZIF-8 reflections decreased, accompanied by an increase in the amorphous background of the polymer-containing samples. SA contributed broad, semicrystalline features at approximately 14–15° and 21–22° in 2θ, whereas PVP produced a characteristic amorphous halo at 20–22° in 2θ. The superposition of these polymer-associated features elevated the background and reduced the apparent

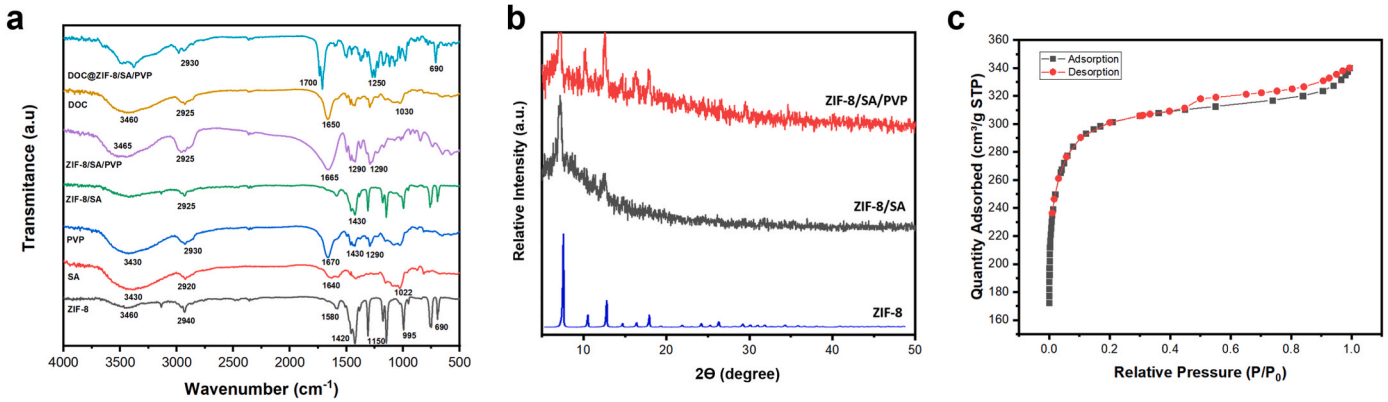


Fig. 1. a) FTIR spectra of DOC, pristine ZIF-8, SA, PVP, ZIF-8/SA, ZIF-8/SA/PVP, and DOC@ZIF-8/SA/PVP. b) XRD patterns of pristine ZIF-8, ZIF-8/SA, and ZIF-8/SA/PVP, showing retention of the characteristic ZIF-8 reflections after polymer incorporation. c) Nitrogen adsorption–desorption isotherm of pristine ZIF-8 at 77 K, displaying the characteristic adsorption behavior of a predominantly microporous material.

prominence of the ZIF-8 reflections in ZIF-8/SA and, more noticeably, in ZIF-8/SA/PVP. This progressive change from pristine ZIF-8 to ZIF-8/SA and ZIF-8/SA/PVP is consistent with successful polymer incorporation without detectable disruption of the crystalline ZIF-8 phase [24]. Overall, the retention of characteristic ZIF-8 peak positions, along with reduced peak intensity and the emergence of a broader amorphous background, supports the successful integration of the SA/PVP polymer matrix with ZIF-8 while preserving the crystalline integrity of the MOF framework. These findings are consistent with the FTIR results, which also indicate preservation of the characteristic ZIF-8 imidazolate framework after polymer incorporation.

3.3. Nitrogen adsorption–desorption analysis (BET)

The N_2 adsorption–desorption isotherm of pristine ZIF-8 at 77 K exhibited a steep uptake at low relative pressures, followed by an early plateau, indicating a predominantly microporous type I(a)-like adsorption profile characteristic of ZIF-8 (Fig. 1c). A slight hysteresis loop was observed at higher relative pressure, which could be attributed mainly to interparticle voids and particle packing effects rather than to intrinsic mesoporosity. BET analysis was performed using data from the adsorption branch over the low-relative-pressure range of P/P_0 = 0.01996–0.06031. The BET plot showed excellent linearity (R^2 = 0.999), with a positive BET constant (CBET = 493.5) and a monolayer capacity of 269.0 cm^3/g STP. The calculated BET surface area was 1171 m^2/g. The total pore volume was 0.522 cm^3/g at $P/P_0 \approx 0.99$, and the t-plot micropore volume was 0.339 cm^3/g. These textural properties confirm that the ZIF-8 core provides substantial accessible microporosity for drug loading, while the SA/PVP polymergate structure is expected to regulate the subsequent release behavior.

3.4. DLS and zeta potential analysis

The DLS intensity-weighted distribution showed a unimodal peak at 184 nm, indicating the absence of detectable large aggregates under the measurement conditions. However, the measured PDI value of 0.447 ± 0.026 indicates moderate polydispersity rather than a narrow or highly uniform size distribution. Therefore, the formulation is best described as having a unimodal intensity peak with moderate polydispersity (Fig. 2a). A hydrodynamic diameter of 150–200 nm falls within the size range commonly reported ZIF-8 nanoparticles used in drug-delivery studies. Polymer functionalization can increase the hydrodynamic diameter, consistent with the formation of an adsorbed shell; such DLS shifts upon surface modification are widely documented [25].

The zeta potential was -27.56 ± 1.2 mV (n = 3, 25 °C; Fig. 2b), a moderately negative value close to the electrostatic stability threshold in the tested medium. A negative zeta potential is expected for alginate-containing shells (deprotonated COO^-), while PVP can screen charge and reduce the magnitude of the zeta potential, consistent with the observed magnitude. PVP capping typically minimizes the magnitude of zeta potential toward neutrality by screening surface charge, a trend

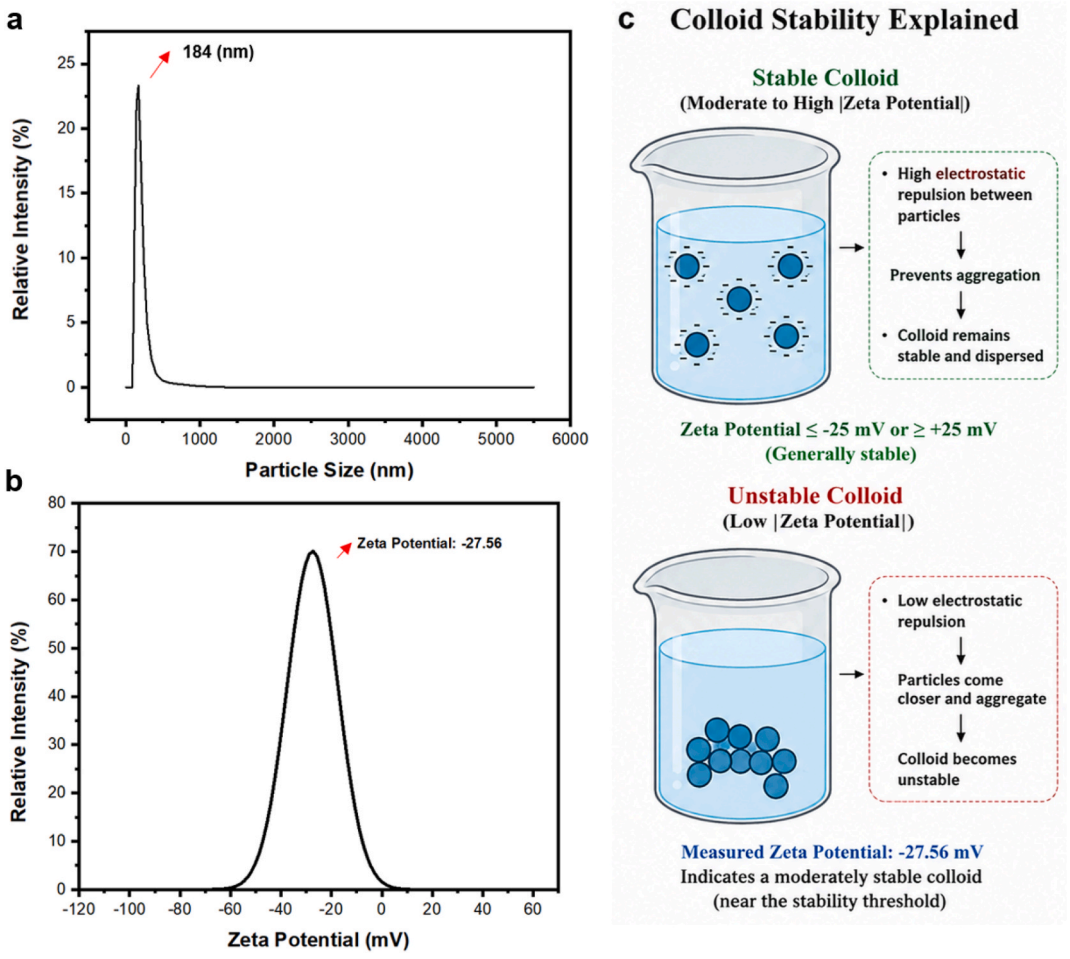


Fig. 2. a,b) Dynamic light scattering (DLS) and zeta potential analysis of the ZIF-8/SA/PVP nanocarrier. The DLS intensity-weighted particle size distribution showed a unimodal peak centered at 184 nm, with moderate polydispersity as indicated by the measured PDI. The zeta potential distribution showed a moderately negative value of −27.56 mV, indicating near-threshold colloidal stability and supporting the presence of deprotonated carboxylate groups from SA. c) Schematic illustration of colloidal stability.

observed across multiple nanoparticle systems and also reported for PVP-modified ZIF-based constructs [26].

3.5. FE-SEM morphology

The observed rhombic dodecahedral morphology and particle-size range of 100–300 nm are consistent with recent reports of ZIF-8 synthesized under comparable solution-phase conditions, which commonly yielded well-faceted rhombic-dodecahedral crystals of approximately 150–200 [27–29]. Particle sizes measured by FE-SEM are expected to be slightly smaller than hydrodynamic diameters because DLS includes the solvation/surface layer and is subject to intensity bias toward larger

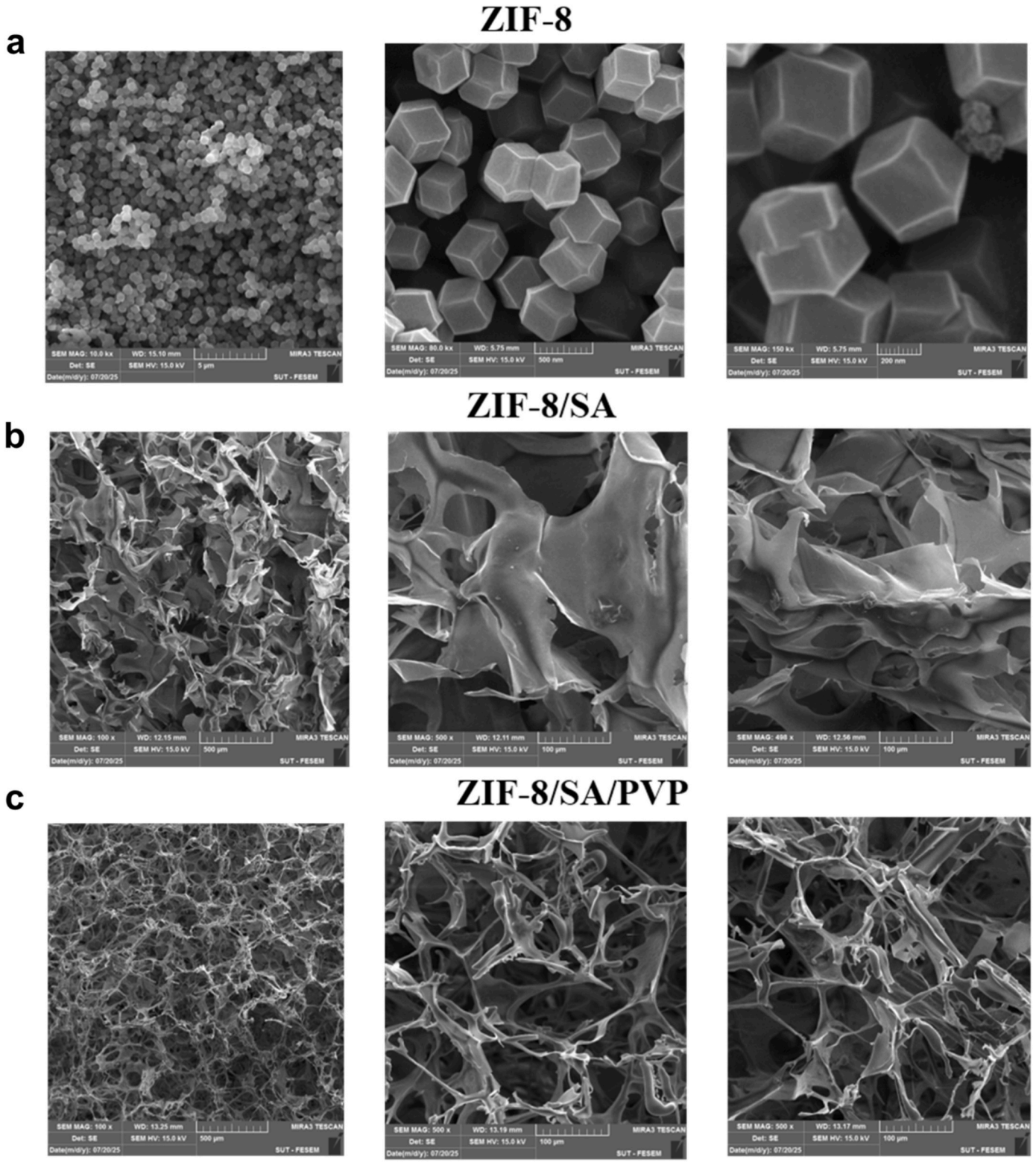


Fig. 3. FE-SEM micrographs of pristine ZIF-8 nanocrystals (top row), ZIF-8/SA composites (middle row), and ZIF-8/SA/PVP composites (bottom row) at various magnifications.

species. Upon SA coating (ZIF-8/SA), individual polyhedra are embedded within a continuous polymer film, and an amorphous matrix obscures interparticle necks. Alginate networks formed by freezing/lyophilization (or rapid dehydration) typically exhibit interconnected macropores and smooth lamellae, which account for the sheet-like regions observed here.

After SA/PVP coating, amorphous films and ligament-like bridges were observed, consistent with a polymer overlayer that masks polyhedral edges (Fig. 3). The ZIF-8 particle uniformity and size window were consistent with canonical ZIF-8 reports, in which rhombic dodecahedral particles range from 100 to 600 nm depending on synthesis time and composition. Similar masking of crystalline cores by amorphous polymer sheaths has been reported in SA/PVP nanocarriers, in which SEM reveals smooth, merged surfaces after polymer addition. For direct numerical comparison, an SA/PVP/γ-Al_2O_3 system exhibited FE-SEM particle sizes of 120.28–187.14 nm (mean = 150 nm), which fall within a similar morphological and size range to that of the ZIF-8 core before polymer coating. In that study, porous surface features with fenestrations of 327–472 nm were also resolved, demonstrating that polymer-inorganic hybrids can exhibit pore-like textures at the nanoscale; the coated films exhibited analogous smoothing and bridging at higher magnification.

3.6. EDS mapping

ZIF-8 showed uniform distributions of Zn and N across the faceted particles, with a detectable C background and a weak O signal, consistent with an imidazolate framework and typical surface species from preparation. After alginate coating, the Na and O signals co-localized with C throughout the films, while the Zn signal remained continuous beneath the polymer layer, indicating polymer deposition without loss of the ZIF-8 cores. In the DOC@ZIF-8/SA/PVP sample, the increased N signal is consistent with PVP incorporation, the distributions of C, O, and Na support the presence of SA in the polymer shell, and the retained spatially overlapping Zn signal confirmed preservation of the ZIF-8 core within the polymeric network (Fig. 4). These compositional maps corroborate FE-SEM evidence for a conformal polymer overlayer.

3.7. pH-responsive release

The DOC@ZIF-8/SA/PVP nanocarrier exhibited a drug loading content (DLC) of 14.5 ± 0.8% and an encapsulation efficiency (EE) of 84.6 ± 2.3%, indicating the successful incorporation of docetaxel into the polymer-gated ZIF-8 nanocarrier system. The relatively high EE value indicates a strong affinity of DOC for the porous ZIF-8 framework and the surrounding SA/PVP matrix, while the resulting DLC confirms the hybrid carrier's effective loading capacity.

DOC@ZIF-8/SA/PVP showed pH-selective release with an initial rapid phase followed by sustained release, reaching 35% at 5 h, 55% at 24 h, 75% at 48 h, 90% at 72 h, and 95% at 96–120 h at pH 5.5. At pH 7.4, the same formulation released 22% at 5 h, 39% at 24 h, 50% at 48 h, and reached a plateau near 59% by 120 h, demonstrating sustained, medium-dependent release control. Bare DOC@ZIF-8 released far less drug: 6% (5 h), 14% (24 h), 22–26% (48–72 h), and 24–25% (120 h) at pH 5.5, consistent with the fact that the SA/PVP overlayer enhances release at acidic pH relative to the uncoated MOF (Fig. 5). At pH 7.4, DOC release from DOC@ZIF-8 remained slow (3–14% up to 120 h), consistent with ZIF-8's higher stability in neutral media compared with acidic or phosphate-rich environments [30]. The SA/PVP shell may reduce burst release at neutral pH and enhance diffusion under acidic conditions through alginate swelling and hydrogen-bond-mediated plasticization of PVP. Comparable SA/PVP carriers (without MOF)

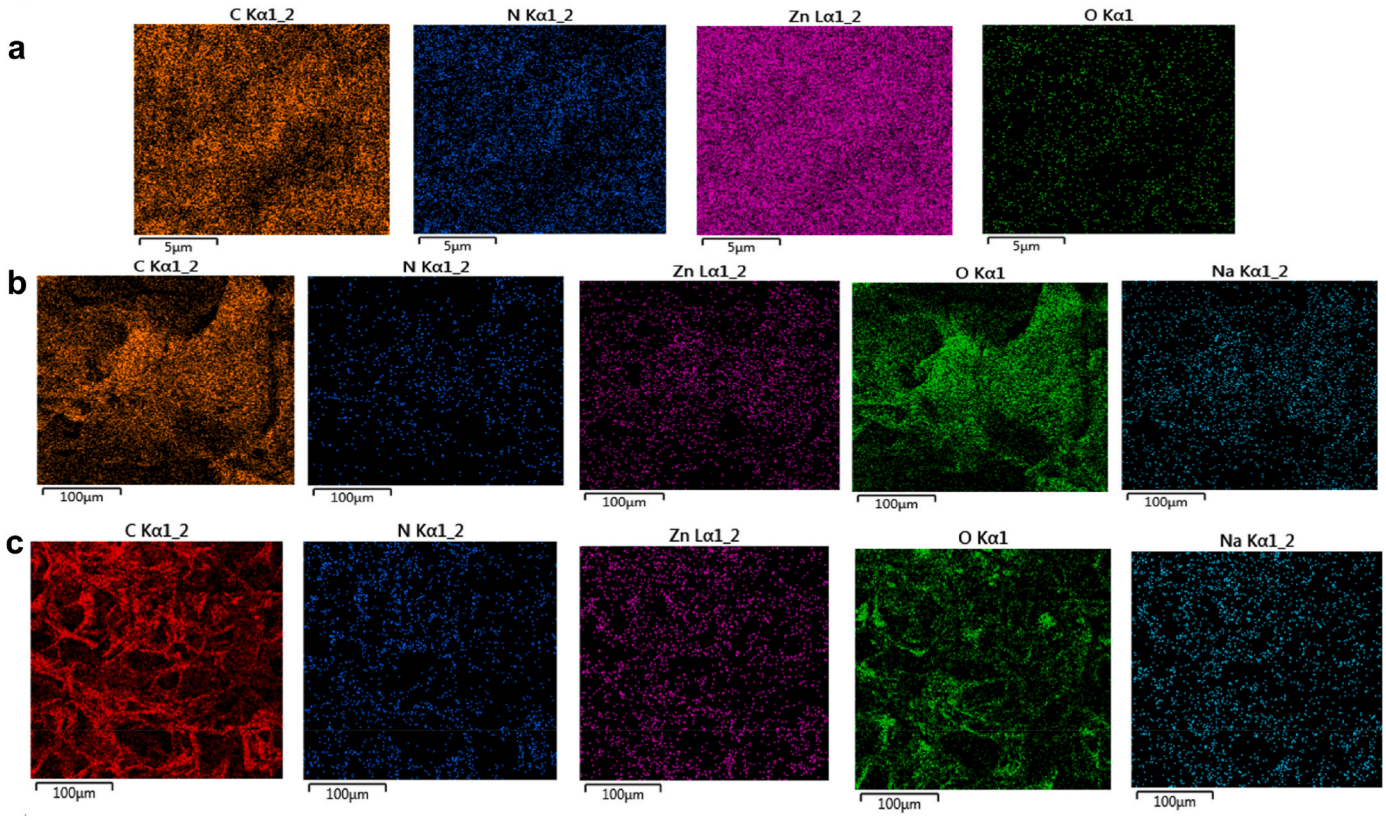


Fig. 4. EDS elemental maps acquired at 15 kV for a) ZIF-8, b) ZIF-8/SA, and c) DOC@ZIF-8/SA/PVP. Channels: C, N, O, Na, Zn. Scale bars: 5 μm in panel a and 100 μm in panels b and c. Maps show uniform Zn/N over ZIF-8 and the emergence of Na/O (alginate) and increased N (PVP) in coated samples, with Zn retained beneath the polymer network.

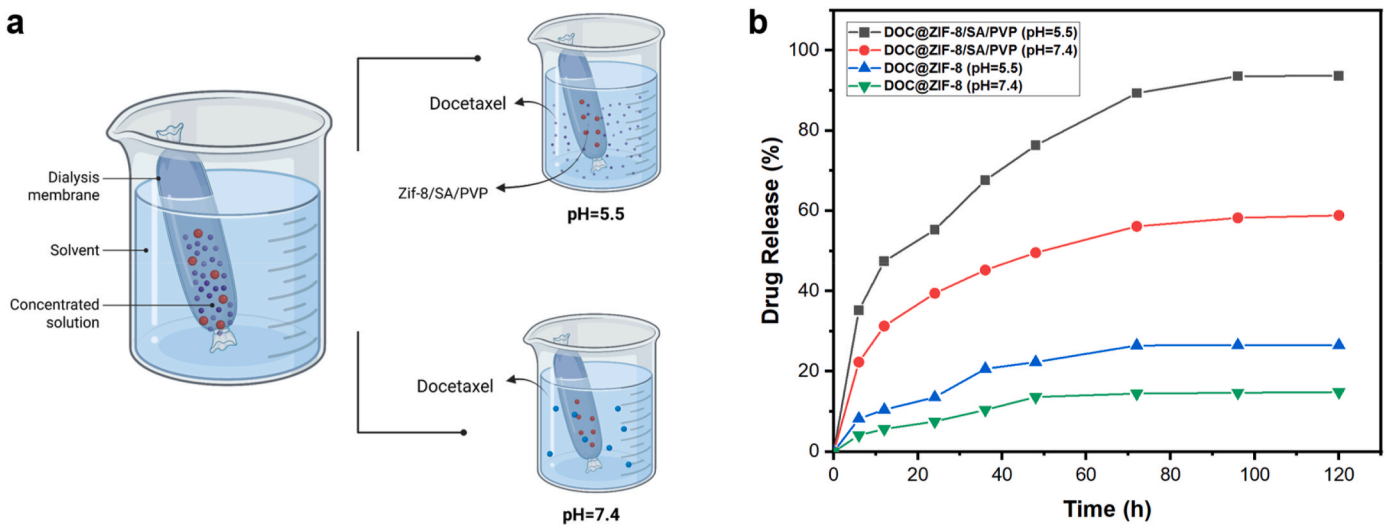


Fig. 5. *In vitro* cumulative release profiles of DOC from the different nanocarrier formulations under physiological conditions at pH 7.4 and acidic endosomal/lysosomal-like conditions at pH 5.5 at 37 °C.

exhibit sustained, pH-dependent release over more than 100 h, with faster kinetics under acidic conditions, providing a direct polymer-only benchmark for the observed pH selectivity. Compared with the SA/PVP/γ-Al_2O_3 benchmark, which reached 98% release at pH 5.5 and 65% at pH 7.4 within 96 h, DOC@ZIF-8/SA/PVP showed comparable acidic release but slightly lower release at neutral-pH, indicating improved retention under physiological conditions while preserving strong acid-triggered release. The comparatively slower release from bare DOC@ZIF-8 suggests that the polymer shell increases wettability and transport pathways while ZIF-8 provides acid-labile storage, yielding a cooperative "polymer gate and MOF reservoir" effect [31]. This apparently counterintuitive behavior can be explained by the physicochemical role of the SA/PVP shell. Although ZIF-8 is intrinsically acid-labile, bare DOC@ZIF-8 may show limited DOC release because of the poor aqueous solubility and hydrophobic nature of DOC, possible DOC aggregation or crystallization within or around the MOF particles, and limited wetting of the uncoated ZIF-8 surface in the release medium. In contrast, the SA/PVP shell may improve water penetration and interfacial wettability, reduce DOC crystallization by maintaining a more highly dispersed drug state, and shift part of the drug population toward polymer-associated or near-surface domains. Under acidic conditions, alginate swelling and weakening of polymer–drug and drug–MOF interactions may further facilitate DOC diffusion, while acid-triggered ZIF-8 destabilization contributes to release from the MOF reservoir. Therefore, the greater release from DOC@ZIF-8/SA/PVP may be attributed to the cooperative effects of improved wettability, altered DOC localization, and pH-responsive polymer-assisted diffusion rather than to ZIF-8 degradation alone.

Several nanocarrier classes have been explored for hydrophobic anticancer drugs, including polymeric nanoparticles, liposomes, micelles, mesoporous inorganic carriers, hydrogel-based systems, and MOF-based platforms. Each class offers specific advantages but also has limitations. Polymeric nanoparticles and micelles generally improve drug solubilization and biocompatibility, but their loading capacity, serum stability, and control of release may be limited [10,32]. Liposomes are clinically established and can reduce systemic toxicity, yet their release behavior is often not intrinsically linked to acidic tumor/endosomal environments unless additional stimuli-responsive components are incorporated [33]. Mesoporous silica and other inorganic carriers offer high surface area and tunable porosity, but concerns about long-term persistence, biodegradability, and biological clearance remain significant [34]. Bare ZIF-8 exhibits high porosity and acid-labile disassembly, but unmodified particles may aggregate, exhibit nonspecific biomolecular interactions, and lack sufficient interfacial control [35].

In comparison with these carrier systems, the principal advantage of the present DOC@ZIF-8/SA/PVP formulation lies in the functional integration of an acid-responsive porous reservoir with a hydrated polymeric gate. The ZIF-8 core provides a high-capacity environment for drug loading and undergoes destabilization under acidic conditions, whereas the SA/PVP layer improves aqueous compatibility, regulates interfacial interactions, and controls drug diffusion. This cooperative architecture reduces DOC release at physiological pH relative to acidic pH. Thus, the proposed system combines the loading and pH-responsive properties of a metal-organic framework with the stabilization and transport-regulating functions of a biocompatible polymer matrix, thereby distinguishing it from carriers based exclusively on either an inorganic porous core or a polymeric platform.

DOC-loaded and hyaluronic acid (HA)-coated ZIF-8 formulations have demonstrated tumor-selective release and enhanced cytocompatibility in leukemia and solid tumor models, supporting the translational rationale for ZIF-8-mediated DOC delivery in breast cancer [36]. As shown in Table 1, this cooperative pH-responsive mechanism is consistent with general pH-responsive delivery principles, in which microenvironmental acidity triggers a switch from retention to release. Across diverse MOF–polymer hybrids, effective drug loading and pronounced pH-accelerated release under acidic conditions have been reported to improve anticancer activity in standard cell models. The DOC@ZIF-8/SA/PVP platform developed in this study showed similar pH-selective release behavior and biological response trends (Table S2).

Table 1 indicates that both MOF-based and polymer-gated carriers have advantages, and that DOC@ZIF-8/SA/PVP combines them. The formulation showed high drug release under acidic conditions (95% at pH 5.5 in 96–120 h) and a more controlled release at pH 7.4 (59% within 120 h). In contrast with the SA/PVP/γ-Al_2O_3 benchmark, which exhibited similarly high release at acidic-pH but higher release at neutral pH, DOC@ZIF-8/SA/PVP showed comparable release at acidic-pH and improved retention under neutral conditions. This reduced release at pH 7.4 may decrease premature drug leakage during circulation, whereas exposure to acidic conditions at pH 5.5 may facilitate drug release in intracellular compartments, particularly endosomes and lysosomes. The SA/PVP-gated formulation released DOC under both pH conditions, whereas bare DOC@ZIF-8 released substantially less DOC over the same period. These comparative findings demonstrate that the performance of DOC@ZIF-8/SA/PVP arises from the complementary functions of its components: ZIF-8 serves as an acid-labile drug reservoir,

Table 1
Comparative cumulative drug-release performance of ZIF-8-based and non-MOF carriers under different pH conditions.

Carrier/Drug	Medium & time window	Cumulative release (reported)	Notes	Source
DOC@ZIF-8/HA (hyaluronic-acid coated)	pH 5.0 vs 7.4; up to 72 h	Higher at pH 5.0 than at 7.4 across the whole window	ZIF-8 core with HA shell; the study also confirms that tumor-like pH accelerates release.	[36]
DOX (pH-sensitive prodrug) @ZIF-8	Acidic vs pH 7.4	Pronounced pH-responsive release; minimal at 7.4, increased in acid	Mineralization of pH-Sensitive DOX Prodrug in ZIF-8	[37]
Curcumin@ZIF-8	pH 5.5 vs 7.4 (overall profile)	Release at pH 5.5 is 6.22× that at 7.4	Quantified ratio reported	[38]
DOX@ZIF-8 (representative MOF example)	pH 5.0–5.5 vs 7.4; 0–48/72 h	Significantly faster in acidic media than at pH 7.4 (multiple ZIF-8 drug systems summarized).	Peer-reviewed review summarizing ZIF-8 pH-responsive release behavior across many datasets.	[39]
ZIF-8 (general stability in biological media)	PBS/serum vs water; hours-days	PBS/biological media accelerate ZIF-8 degradation compared with pure water; acidic pH also speeds disassembly.	Useful for interpreting medium effects (e.g., phosphate-induced breakdown).	[40]
Alginate/PVP polymer carriers (MOF-free, benchmark)	Acidic vs neutral buffers; 0–96/120 h (various drugs)	Sustained, pH-dependent release; typically faster under mildly acidic conditions than at 7.4.	Shows the polymer matrix alone can be pH-responsive (baseline for the SA/PVP shell).	[41]
pH-sensitive polymeric micelles (non-MOF, DOC analog)	pH-triggered; ≤48–72 h	Acidic pH increases release/switches to an "on" state compared to neutral pH, thereby improving cytocompatibility *in vitro*.	Representative for hydrophobic taxanes (PTX/DOC-like); supports the trigger concept.	[42]
PTX micelles (non-MOF control)	pH 5.5 vs 7.4 48 h	92% (5.5) vs 50% (7.4)	pH-responsive taxane benchmark outside MOFs	[43]
RhB@ZIF-8	pH 4.0 48 h/120 h	92.6%/99.3%	Shows acid-driven ZIF-8 disassembly and full release	[44]
General ZIF-8 drug cargo	pH 7.4 vs 5–6	Typical pattern: little release at pH 7.4, strong/accelerated in acid	Comprehensive biomedical review	[45]
DOC@ZIF-8/SA/PVP	pH 5.5, 0–120 h	35% (5 h), 55% (24 h), 75% (48 h), 90% (72 h), 95% (96–120 h)	pH-selective release with an initial rapid phase and sustained profile	This work
DOC@ZIF-8/SA/PVP	pH 7.4, 0–120 h	22% (5 h), 39% (24 h), 50% (48 h), plateau 59% (120 h)	Controlled release under neutral conditions	This work
DOC@ZIF-8 (bare)	pH 5.5, 0–120 h	6% (5 h), 14% (24 h), 22–26% (48–72 h), 24–25% (120 h)	Much slower without SA/PVP	This work
DOC@ZIF-8 (bare)	pH 7.4, 0–120 h	3–14% (overall)	Very slow in neutral	This work

whereas SA/PVP functions as a hydrated diffusion-regulating gate, together enabling preferential and sustained release under acidic conditions.

The acidic release profile is a cooperative process involving both the MOF reservoir and the polymer gate. Previous studies have shown that ZIF-8 is relatively stable under neutral conditions but susceptible to degradation in acidic media due to protonation of the 2-methylimidazolate linkers, which weakens Zn–N bonding and promotes framework disassembly [46,47]. Therefore, the ZIF-8 core is expected to progressively destabilize at pH 5.5. This process may increase DOC mobility within the MOF reservoir and promotes release under acidic conditions. The SA/PVP coating modulates mass transport in parallel. The SA component can increase hydration and pH-dependent swelling, and PVP can increase water uptake and hydrogen bonding between polymer chains, leading to plasticization. These effects increase shell permeability and create hydrated pathways for DOC transport after partial ZIF-8 destabilization. Thus, the observed release arises from cooperative destabilization of ZIF-8 and gated diffusion through the hydrated SA/PVP shell, rather than from MOF-core disassembly alone. The greater amount of DOC released from DOC@ZIF-8/SA/PVP than from bare DOC@ZIF-8 under acidic conditions is consistent with this interpretation. It is also supported by the slower release at pH 7.4, where ZIF-8 degradation is reduced and polymer-gate permeability may be lower.

3.8. Kinetic modeling of drug release

The release profiles were fitted to zero-order, first-order, Higuchi, and Korsmeyer–Peppas kinetic models to identify the dominant release mechanism (Fig. 6 and Table 2). For DOC@ZIF-8/SA/PVP, the Korsmeyer–Peppas model provided the best fit, with R^2 values of 0.984 at pH 5.5 and 0.975 at pH 7.4. The Higuchi model showed weaker fits, with R^2 values of 0.948 and 0.927 at pH 5.5 and 7.4, respectively, while the first-order model showed comparable or weaker fits of 0.959 and 0.822. The zero-order model showed the weakest fit, with R^2 values of 0.763 and 0.755. A similar model-ranking trend was observed for bare DOC@ZIF-8, with the Korsmeyer–Peppas model yielding R^2 values of 0.930 at pH 5.5 and 0.915 at pH 7.4. The release exponent values ranged from $n = 0.33$ to 0.42 across all formulations, which are below the Case I threshold for spherical matrices ($n < 0.45$) and indicate a predominantly Fickian, diffusion-controlled release mechanism. DOC release likely proceeds through intracrystalline transport within ZIF-8 micropores and diffusion across the hydrated SA/PVP polymer shell. Under acidic conditions, weakening of Zn–N coordination and increased polymer-shell permeability may increase the effective diffusivity of DOC. For the Korsmeyer–Peppas analysis, only the initial release region corresponding to $M_t/M_\infty < 0.60$ was used, and k and n were obtained from the linearized equation $\log(M_t/M_\infty) = \log k + n \log t$. Analyses restricted to this initial release region, together with supplementary diagnostics, including residuals, adjusted R^2, AIC/BIC, and nonlinear least-squares fitting, yielded the same model-ranking trend.

3.9. Cytotoxicity analysis

MTT assays were performed in MCF-7 and NIH3T3 cells to evaluate free DOC, DOC@ZIF-8, and DOC@ZIF-8/SA/PVP ($n = 3$, mean ± SD; one-way ANOVA followed by Tukey's post hoc test). At DOC-equivalent concentrations of 3.625–10.875 μg/mL, DOC@ZIF-8/SA/PVP generally preserved higher cell viability than free DOC in both cell lines. At 14.5–36.25 μg/mL, DOC@ZIF-8/SA/PVP produced a concentration-dependent reduction in MCF-7 cell viability, while NIH3T3 cell viability remained comparatively higher. At concentrations of ≥72.5 μg/mL, viability declined in both cell lines (Fig. 7). Pristine ZIF-8 showed noticeable cytotoxicity at higher doses, whereas SA and PVP alone were biocompatible across the tested range. To minimize nanoparticle-assay interference, acellular interference controls,

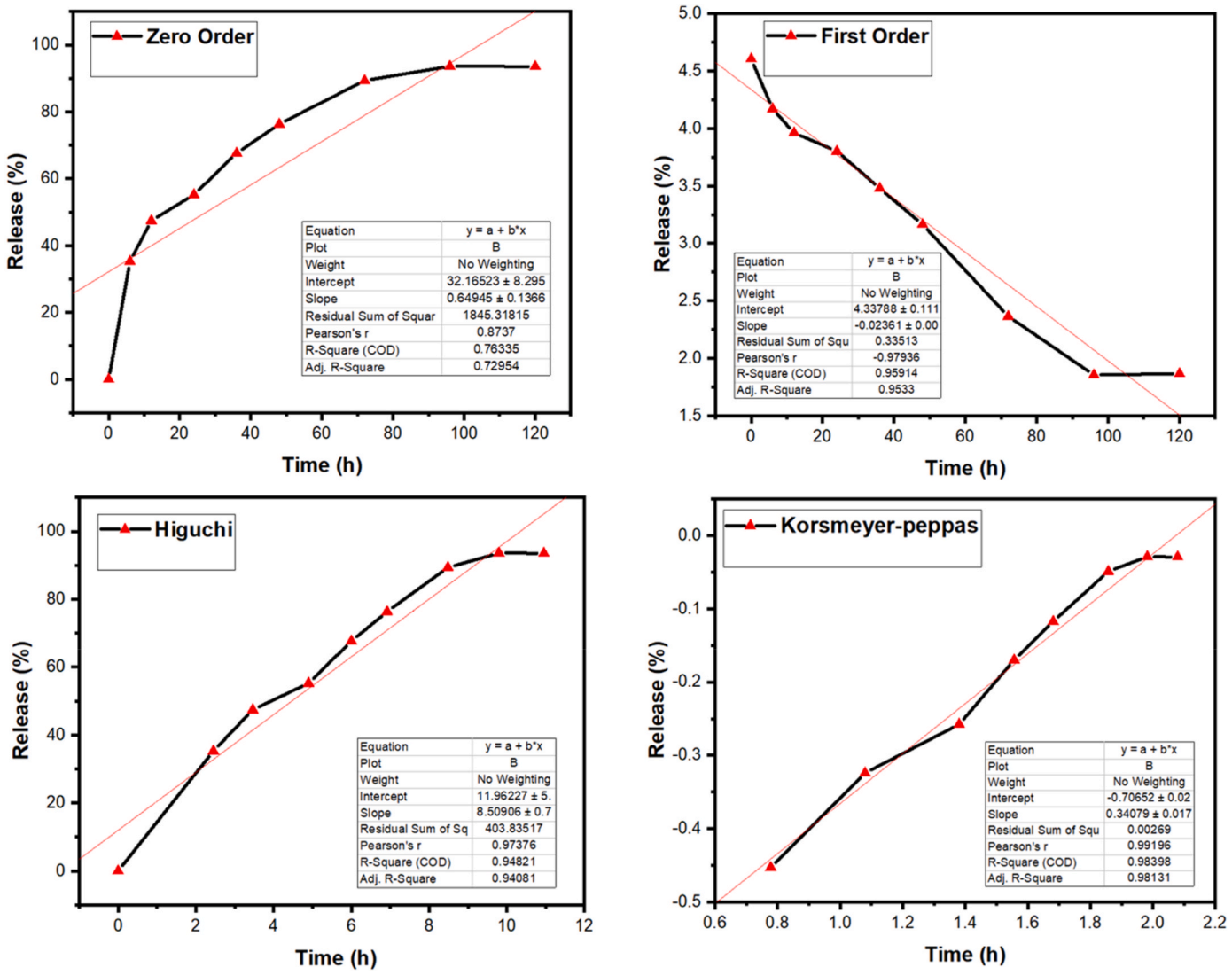


Fig. 6. Kinetic modeling of DOC release from DOC@ZIF-8/SA/PVP nanocarriers at pH 5.5. The cumulative release data were fitted to a) zero-order, b) first-order, c) Higuchi, and d) Korsmeyer–Peppas models to elucidate the dominant release mechanism.

Table 2
Kinetic-model fitting parameters for DOC release from DOC@ZIF-8/SA/PVP and DOC@ZIF-8 at pH 5.5 and pH 7.4.

Formulations	Zero-order	First-order	Higuchi	R^2	Korsmeyer–Peppas		Release mechanism
	R^2	R^2	R^2		k	n	
DOC@ZIF-8/SA/PVP (pH=5.5)	0.7633	0.9591	0.9482	0.984	0.2020	0.3408	Fickian diffusion
DOC@ZIF-8/SA/PVP (pH=7.4)	0.7548	0.8215	0.9271	0.9747	0.1337	0.329	Fickian diffusion
DOC@ZIF-8 (pH=5.5)	0.7203	0.7382	0.9065	0.9299	0.0394	0.4196	Fickian diffusion/near boundary
DOC@ZIF-8 (pH=7.4)	0.6882	0.6947	0.8811	0.9154	0.0201	0.434	Near Fickian-anomalous boundary

including carrier-only and MTT/formazan controls, were measured and subtracted from the sample signals. Four-parameter logistic fits showed a higher IC_{50} for DOC@ZIF-8/SA/PVP than for free DOC in MCF-7 cells, as well as a higher IC_{50} than free DOC in NIH3T3 fibroblasts. These results indicate reduced normal-cell toxicity and a cancer/normal-cell response window, but not greater selectivity than free DOC, as indicated by the calculated selectivity index.

The IC_{50} values were calculated from dose–response curves using nonlinear regression analysis based on a four-parameter logistic model. In MCF-7 cells, the IC_{50} values were 4.299 μg/mL for free DOC (95% CI: 4.058–4.541), 13.635 μg/mL for DOC@ZIF-8 (95% CI: 12.305–14.965), and 28.370 μg/mL for DOC@ZIF-8/SA/PVP (95% CI: 24.803–31.936). In NIH3T3 cells, the IC_{50} values were 53.813 μg/mL for free DOC (95% CI: 45.500–62.126), 80.325 μg/mL for DOC@ZIF-8 (95% CI: 58.346–102.304), and 122.740 μg/mL for DOC@ZIF-8/SA/PVP (95% CI: 68.352–177.128). Because a higher IC_{50} indicates lower potency, these data do not support greater cytotoxic potency of DOC@ZIF-8/SA/PVP than free DOC in MCF-7 cells. Instead, the results demonstrate a differential response between cancer and normal cells, as DOC@ZIF-8/SA/PVP showed a higher IC_{50} in NIH3T3 fibroblasts than in MCF-7 cancer cells. The calculated selectivity indices, defined as IC_{50}(NIH3T3)/IC_{50}(MCF-7), were 12.52 for free DOC, 5.89 for DOC@ZIF-8, and 4.33 for DOC@ZIF-8/SA/PVP. Therefore, the main advantages of DOC@ZIF-8/SA/PVP are controlled pH-responsive

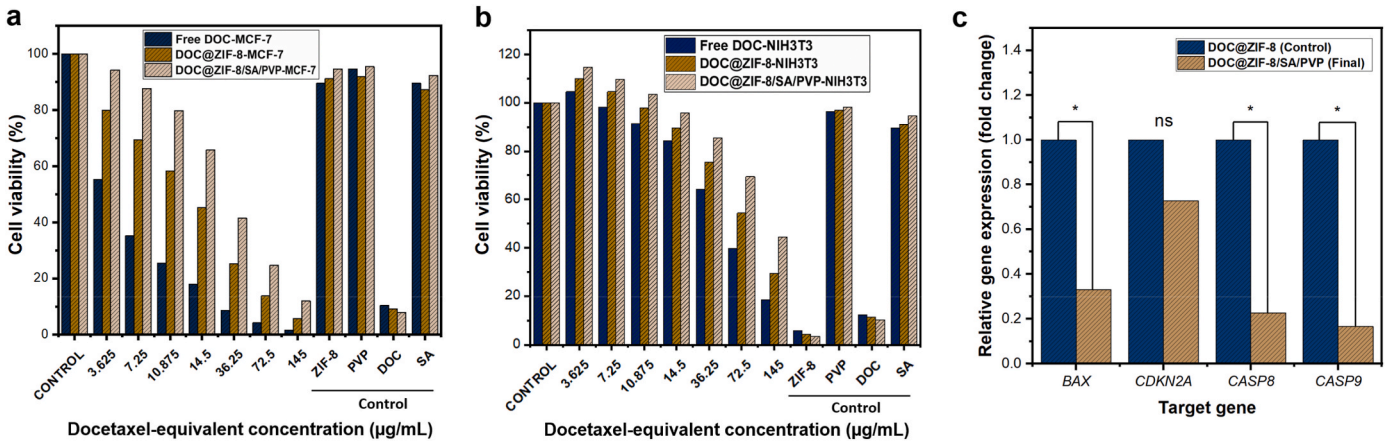


Fig. 7. Cytotoxicity and apoptosis-related gene expression following treatment with DOC formulations. a, b) Viability of MCF-7 breast cancer cells and NIH3T3 fibroblasts, respectively, after treatment with free DOC, DOC@ZIF-8, or DOC@ZIF-8/SA/PVP. DOC@ZIF-8/SA/PVP showed reduced toxicity toward NIH3T3 cells and a cancer/normal-cell response window, but not greater potency than free DOC based on IC_{50} values. c) Relative expression of apoptosis-related genes (*BAX*, *CDKN2A*, *CASP8,* and *CASP9*) in MCF-7 cells treated with DOC@ZIF-8/SA/PVP relative to DOC@ZIF-8 control, as determined by RT-qPCR. Data are presented as mean ± SD (n = 3). Statistical significance was assessed by one-way ANOVA followed by Tukey's post hoc test (*$p < 0.05$; ns: not significant).

delivery and reduced normal-cell toxicity rather than greater intrinsic potency or selectivity relative to free DOC. Based on the measured DLC of 14.5 ± 0.8%, the formulation IC_{50} of 28.370 μg/mL corresponds to an approximate DOC-equivalent IC_{50} of 4.11 μg/mL in MCF-7 cells after 48 h, which is close to the IC_{50} of free DOC under the same conditions.

3.10. Apoptosis-related gene expression after DOC@ZIF-8/SA/PVP treatment

The mRNA expression levels were quantified by RT-qPCR using *B2M* as the reference gene and expressed as fold changes relative to the

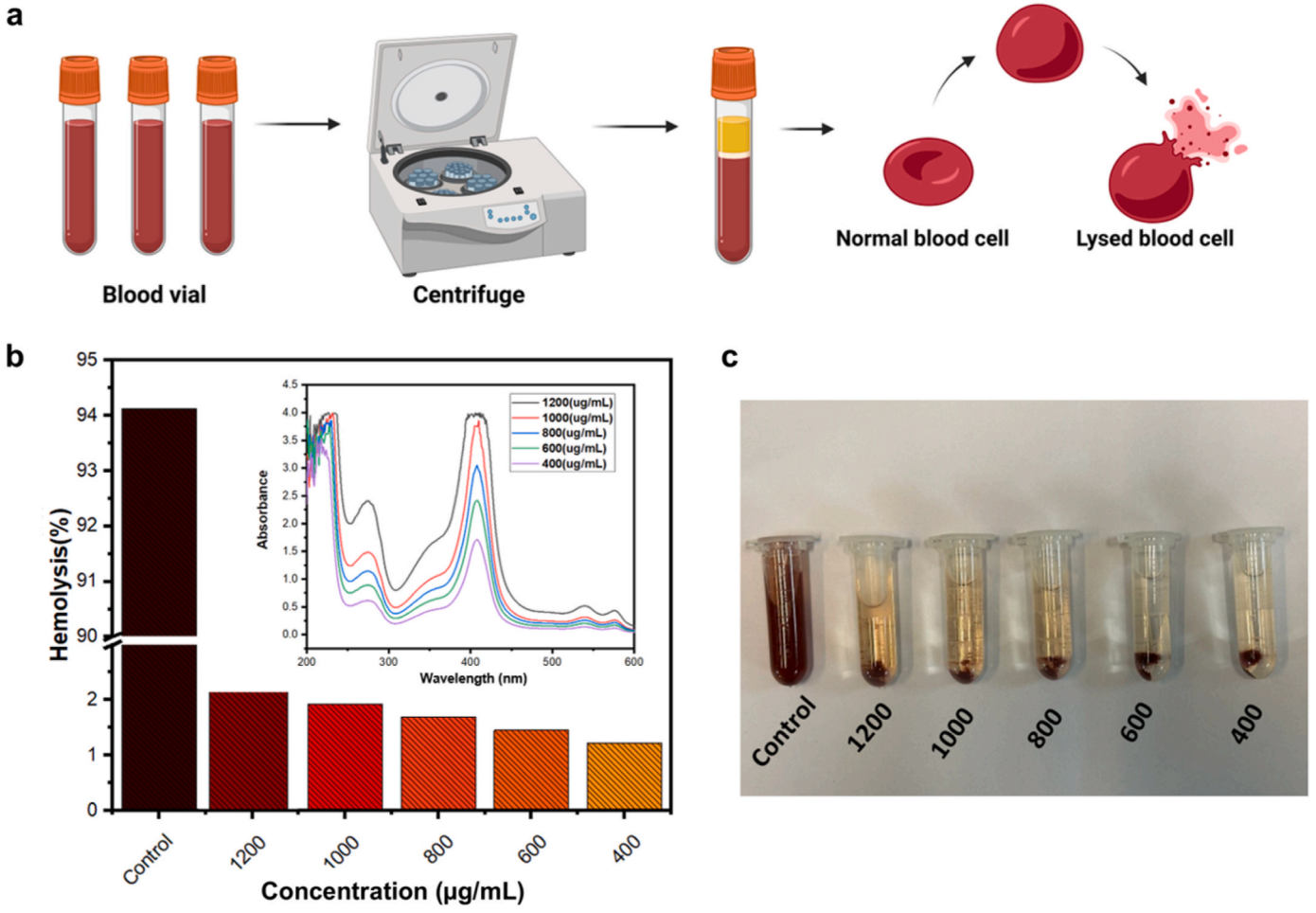


Fig. 8. Hemolysis test. a) Schematic of the assay: RBCs are exposed to the sample and to controls. b) Hemolysis (%) for DOC@ZIF-8/SA/PVP at 400–1200 μg/mL. Triton X-100 produced 94% hemolysis (positive control). c) Representative images of hemolysis samples for different concentrations.

DOC@ZIF-8 control group (mean fold change; 95% CI). *BAX* (0.33; 0.29–0.36; $p < 0.001$), *CASP8* (0.23; 0.21–0.24; $p < 0.001$), and *CASP9* (0.17; 0.15–0.19; $p < 0.001$) were downregulated following DOC@ZIF-8/SA/PVP treatment, whereas *CDKN2A* (p16) did not change significantly. Importantly, the RT-qPCR data did not demonstrate upregulation of the evaluated pro-apoptotic transcripts. Therefore, the present gene-expression results do not support transcriptional activation of apoptosis at the mRNA level under the experimental conditions examined. However, these results do not rule out apoptosis, as DOC-induced apoptosis in MCF-7 cells may be reflected more directly by protein activation and cleavage events than by increased mRNA expression at the sampled time point. The observed decreases in transcript levels could also be due to a timing effect (late apoptosis), mRNA degradation in dying cells, or feedback regulation. Definitive pathway inference, therefore, requires protein-level and functional readouts (e.g., cleaved PARP, cleaved caspase-7, Annexin V/PI staining, or mitochondrial membrane potential assays).

3.11. Hemocompatibility test

The hemolytic activity of DOC@ZIF-8/SA/PVP was evaluated using phosphate-buffered saline (PBS) as the negative control and Triton X-100 as the positive control. Across a concentration range of 400–1200 μg/mL, the formulation induced low hemolysis, increasing from approximately 1.0 ± 0.2% at 400 μg/mL to approximately 2.0 ± 0.3% at 1200 μg/mL (n = 3). These values remained at or below the 2% threshold typically used to define a non-hemolytic material (Fig. 8). The Triton X-100 control produced 94–95% hemolysis, confirming assay responsiveness, while PBS remained at baseline (used for normalization). UV-Vis traces showed the expected oxyhemoglobin features (a Soret band near 415 nm and broad bands around 540–575 nm), and the signal intensity increased consistently with the measured hemolysis. Overall, DOC@ZIF-8/SA/PVP showed acceptable hemocompatibility under the *in vitro* conditions tested.

4. Conclusion

This study aimed to develop a biocompatible and microenvironment-responsive platform for the sustained delivery of docetaxel by integrating an acid-labile ZIF-8 reservoir with a sodium alginate/polyvinylpyrrolidone diffusion-regulating gate. Comprehensive physicochemical characterization verified successful polymer functionalization, preservation of the crystalline framework, effective drug incorporation, and formation of a stable hybrid nanostructure. The polymer-gated architecture promoted preferential and sustained docetaxel release under acidic conditions while restricting premature drug liberation under physiological conditions, reflecting the cooperative contributions of framework destabilization, enhanced matrix hydration, and diffusion through the polymeric barrier. Release kinetic analysis further supported a predominantly diffusion-governed transport mechanism. Biological evaluation demonstrated that the formulation maintained cytotoxic activity against breast cancer cells while reducing toxicity toward normal fibroblasts relative to free docetaxel under the tested conditions. The formulation also exhibited satisfactory hemocompatibility under the investigated conditions. These findings establish the sodium alginate/polyvinylpyrrolidone-gated ZIF-8 system as a promising strategy for controlled and pH-selective docetaxel delivery, although further *in vivo* investigation is necessary to determine its pharmacokinetic performance, biodistribution, therapeutic efficacy, and long-term safety.

Abbreviation	Full form
DOC	docetaxel
ZIF-8	zeolitic imidazolate framework-8
MOF	metal–organic framework
SA	sodium alginate
PVP	polyvinylpyrrolidone
HER2	human epidermal growth factor receptor 2
EPR	enhanced permeability and retention
TME	tumor microenvironment
HA	hyaluronic acid
Hmim	2-methylimidazole
PBS	phosphate-buffered saline
DMEM	Dulbecco's modified Eagle medium
FBS	fetal bovine serum
MTT	3-(4,5-dimethylthiazol-2-yl)-2,5-diphenyltetrazolium bromide
DMSO	dimethyl sulfoxide
FTIR	Fourier-transform infrared spectroscopy
XRD	X-ray diffraction
DLS	dynamic light scattering
PDI	polydispersity index
FE-SEM	field-emission scanning electron microscopy
EDS	energy-dispersive X-ray spectroscopy
BET	Brunauer–Emmett–Teller
DLC	drug loading content
EE	encapsulation efficiency
UV–Vis	ultraviolet–visible
SD	standard deviation
ANOVA	analysis of variance
IC_{50}	half-maximal inhibitory concentration
RNA	ribonucleic acid
cDNA	complementary deoxyribonucleic acid
RT-qPCR	reverse-transcription quantitative polymerase chain reaction
BAX	BCL2-associated X apoptosis regulator
CDKN2A	cyclin-dependent kinase inhibitor 2A
CASP8	caspase-8
CASP9	caspase-9
B2M	beta-2-microglobulin
RBCs	red blood cells
HP	hemolysis percentage
PC	positive control
NC	negative control

Ethics approval and consent to participate

Commercially available human red blood cells were used for the hemolysis assay. No identifiable human samples or personal data were collected in this study. Therefore, ethics approval was not required under the institutional guidelines of the Pasteur Institute of Iran (IPI).

Funding

This research did not receive any specific grant from funding agencies in the public, commercial, or not-for-profit sectors.

CRediT authorship contribution statement

Sepideh Asadi: Conceptualization, Data curation, Formal analysis, Investigation, Visualization, Writing – original draft. **Iman Barzgar:** Formal analysis, Investigation, Methodology, Software, Writing – original draft. **Arman Barzgar:** Formal analysis, Investigation, Methodology, Software, Writing – original draft. **Hanieh Eftekhari:** Data curation, Investigation, Resources. **Leila Jamei:** Data curation, Formal analysis, Visualization. **Fatemeh Hasibi:** Investigation, Validation, Writing – review & editing. **Yavuz Nuri Ertas:** Conceptualization, Funding acquisition, Methodology, Project administration, Supervision, Visualization, Writing – review & editing.

Declaration of competing interests

The authors declare that they have no known competing financial interests or personal relationships that could have appeared to influence the work reported in this paper.

Acknowledgments

The authors used Grammarly to assist with grammar checking and improve the manuscript's academic quality during preparation. The authors have reviewed and edited the manuscript as necessary and take full responsibility for its content. Y.N.E. acknowledges support from the Health Institutes of Türkiye (TÜSEB) Incentive Award, the Turkish Academy of Sciences Distinguished Young Scientist Award (TÜBA-GEBİP), and the Scientific and Technological Research Council of Türkiye (TÜBİTAK) Incentive Award.

Appendix A. Supplementary data

Supplementary data to this article can be found online at https://doi.org/10.1016/j.jddst.2026.108800.

Data availability

Data will be made available on request.

References

[1] Far B. Farasati, M. Omrani, M.R. Naimi Jamal, S. Javanshir, Multi-responsive chitosan-based hydrogels for controlled release of vincristine, Commun. Chem. 6 (1) (2023) 28.
[2] Z.K. Gu, Z.C. Guo, S. Gao, L.R. Huang, Z. Liu, Hierarchically structured molecularly imprinted nanotransducers for truncated HER2-Targeted photodynamic therapy of therapeutic antibody-resistant breast cancer, ACS Nano 17 (11) (2023) 10152–10163.
[3] H. Nosrati, M. Salehiabar, J. Charmi, K. Yaray, M. Ghaffarlou, E. Balcioglu, Y. N. Ertas, Enhanced in vivo radiotherapy of breast cancer using gadolinium oxide and gold hybrid nanoparticles, ACS Appl. Bio Mater. 6 (2) (2023) 784–792.
[4] R. Patel, P. Klein, A. Tiersten, J.A. Sparano, An emerging generation of endocrine therapies in breast cancer: a clinical perspective, Npj Breast Cancer 9 (1) (2023).
[5] X. Xiong, L.W. Zheng, Y. Ding, Y.F. Chen, Y.W. Cai, L.P. Wang, et al., Breast cancer: pathogenesis and treatments, Signal Transduct Tar 10 (1) (2025).
[6] J.J. Souchek, A. Laliwala, L. Houser, L. Muraskin, Q. Vu, A.M. Mohs, Fatty acid synthase inhibitors enhance microtubule-stabilizing and microtubule-destabilizing drugs in taxane-resistant prostate cancer cells, Acs Pharmacol Transl 6 (12) (2023) 1859–1869.
[7] T.I. Hsu, Y.P. Chen, R.L. Zhang, Z.A. Chen, C.H. Wu, W.C. Chang, et al., Overcoming the blood-brain tumor barrier with docetaxel-loaded mesoporous silica nanoparticles for treatment of temozolomide-resistant glioblastoma, Acs Appl Mater Inter 16 (17) (2024) 21722–21735.
[8] M. Aalhate, S. Mahajan, R. Kumar, A. Kumar, B. Jangir, S. Munagalasetty, et al., Chondroitin sulfate-mediated targeted delivery of docetaxel and silibinin-loaded nanoparticles for amelioration of anticancer efficacy in breast cancer, ACS Appl. Bio Mater. 8 (9) (2025) 8126–8145.
[9] Y. Li, Y.N. Ertas, A. Jafari, M. Taheri, Y. Pilehvar, Co-delivery of curcumin and chrysin through pH-sensitive hyaluronan-modified hollow mesoporous silica nanoparticles for enhanced synergistic anticancer efficiency against thyroid cancer cells, J. Drug Deliv. Sci. Technol. 87 (2023).
[10] W. Gao, A. Bigham, M. Ghomi, A. Zarrabi, N. Rabiee, M.R. Saeb, et al., Micelle-engineered nanoplatforms for precision oncology, Chem. Eng. J. 495 (2024).
[11] M. Entezari, G.G.Y. Abad, B. Sedghi, R. Ettehadi, S. Asadi, R. Beiranvand, et al., Gold nanostructure-mediated delivery of anticancer agents: biomedical applications, reversing drug resistance, and stimuli-responsive nanocarriers, Environ. Res. 225 (2023).
[12] N. He, W. Li, T. Shi, Z. Li, F. Guo, Z. Li, X. Zhao, Modulated growth of MOFs to fabricate ZIF-8@ chitosan/polyvinylpyrrolidone hydrogels with improved adsorption capacity for CO2, ACS Appl. Polym. Mater. 6 (5) (2024) 2814–2822.
[13] S. Rajeev, K.T.N. Hasoon, U.G. Panicker, Sodium alginate/polyvinylpyrrolidone/lapatinib-loaded Zr-metal organic framework: biocompatibility evaluation and pH-responsive drug release for oral delivery applications, J. Mater. Chem. B 13 (38) (2025) 12205–12223.
[14] M. Pourmadadi, A.R. Hafezi, S. Mafirad, M. Nouri, M. Shirazi, M. Younesi, et al., Development and evaluation of SA/PVP/γ-Al_2O_3 nanocarriers for targeted delivery of curcumin in colon cancer therapy, J. Drug Deliv. Sci. Technol. 105 (2025) 106632.
[15] R. Surya, M.D. Mullassery, N.B. Fernandez, D. Thomas, Synthesis and characterization of a clay-alginate nanocomposite for the controlled release of 5-Flurouracil, J. Sci. Adv. Mater. Devices 4 (3) (2019) 432–441.
[16] N. Jan, A. Madni, S. Khan, H. Shah, F. Akram, A. Khan, et al., Biomimetic cell membrane-coated poly(lactic-glycolic acid) nanoparticles for biomedical applications, Bioeng. Transl. Med. 8 (2) (2023).
[17] L.S. Schwartzberg, R.M. Navari, Safety of Polysorbate 80 in the oncology setting, Adv. Ther. 35 (6) (2018) 754–767.
[18] H. Nosrati, M. Salehiabar, F. Mozafari, J. Charmi, N. Erdogan, M. Ghaffarlou, et al., Preparation and evaluation of bismuth sulfide and magnetite-based theranostic nanohybrid as drug carrier and dual MRI/CT contrast agent, Appl. Organomet. Chem. 36 (11) (2022).
[19] Y. Esmaeili, A. Dabiri, F. Mashayekhi, I. Rahimmanesh, E. Bidram, S. Karbasi, et al., Smart co-delivery of plasmid DNA and doxorubicin using MCM-chitosan-PEG polymerization functionalized with MUC-1 aptamer against breast cancer, Biomed. Pharmacother. 173 (2024).
[20] M. Salehiabar, M. Ghaffarlou, A. Mohammadi, N. Mousazadeh, H. Rahimi, F. Abhari, et al., Targeted CuFe2O4 hybrid nanoradiosensitizers for synchronous chemoradiotherapy, J. Contr. Release 353 (2023) 850–863.
[21] B. Colak, Y.N. Ertas, Implantable, 3D-Printed alginate scaffolds with bismuth sulfide nanoparticles for the treatment of local breast cancer via enhanced radiotherapy, Acs Appl Mater Inter 16 (13) (2024) 15718–15729.
[22] B. Colak, M.C. Cihan, Y.N. Ertas, 3D-Printed, implantable Alginate/CuS nanoparticle scaffolds for local tumor treatment via synergistic photothermal, photodynamic, and chemodynamic therapy, ACS Appl. Nano Mater. 6 (17) (2023) 16076–16085.
[23] J. Cravillon, C.A. Schröder, R. Nayuk, J. Gummel, K. Huber, M. Wiebcke, Fast nucleation and growth of ZIF-8 nanocrystals monitored by time-resolved in situ small-angle and wide-angle X-ray scattering, Angew Chem. Int. Ed. Engl. 50 (35) (2011) 8067–8071.
[24] A. Newman, D. Engers, S. Bates, I. Ivanisevic, R.C. Kelly, G. Zografi, Characterization of amorphous API:Polymer mixtures using X-ray powder diffraction, J. Pharmaceut. Sci. 97 (11) (2008) 4840–4856.
[25] X. Chen, S.M. Argandona, F. Melle, N. Rampal, D. Fairen-Jimenez, Advances in surface functionalization of next-generation metal-organic frameworks for biomedical applications: design, strategies, and prospects, Chem 10 (2) (2024) 504–543.
[26] X. Jiang, J.C. Pan, Z.C. Gong, S.X. Meng, Near-infrared-responsive metal-organic Framework@NaLnF4 upconversion nanoparticle heterostructures for advanced photodynamic theranostics, Acs Appl Mater Inter 17 (29) (2025) 41816–41824.
[27] S.A. Polash, A. Poddar, F. Ahmady, G. Kannourakis, A. Jayachandran, R. Shukla, Impact of ligand concentration on the properties of nucleic-acid-encapsulated MOFs and inflammation modulation in prostate cancer cells, ACS Appl. Bio Mater. 7 (11) (2024) 7635–7645.
[28] M.D. Sosa, C.M.S. Alvares, T. Soteras, I.K. Levy, R. Semino, R.M. Negri, Preparation and comparison of merit parameters of hydrophobic membranes on metal meshes based on ZIF-8/PVDF and in situ formation of ZIF-8 by secondary growth and electrochemical synthesis, ACS Appl. Polym. Mater. 6 (22) (2024) 13552–13566.
[29] E. Amayuelas, J. Farrando-Perez, A. Missyul, Y. Grosu, J. Silvestre-Albero, C. Carrillo-Carrión, Fluorinated nanosized zeolitic-imidazolate frameworks as potential devices for mechanical energy storage, Acs Appl Mater Inter 16 (35) (2024) 46374–46383.
[30] E.A.M.S. Obaid, C. Yu, Y.C. Ma, H.L. Yang, Z.F. Fu, Exploring the efficacy of pH-Responsive Vancomycin/Ag/ZIF-8 nanoparticles modified with hyaluronic acid for enhanced antibacterial therapy and wound healing, Acs Appl Mater Inter 16 (48) (2024) 65942–65954.
[31] A. Chinnathambi, S.A. Alharbi, M. Ramar, P. Arulselvan, S. Muthusami, Fabrication of folic acid-embedded aminated drug encapsulated zeolitic imidazolate framework as promising drug delivery system for lung cancer, J. Mater. Res. 39 (10) (2024) 1537–1547.
[32] M.R.H. Khan, Z. Armstrong, M. Lenertz, B. Saenz, N. Kale, Q.B. Li, et al., Metal-organic framework induced stabilization of proteins in polymeric nanoparticles, Acs Appl Mater Inter 16 (12) (2024) 14405–14420.
[33] M. Hashemi, F. Ghadyani, S. Hasani, Y. Olyaee, B. Raei, M. Khodadadi, et al., Nanoliposomes for doxorubicin delivery: reversing drug resistance, stimuli-responsive carriers and clinical translation, J. Drug Deliv. Sci. Technol. 80 (2023).
[34] Z.H. Zhang, X. Zhang, Y.H. Hao, Y.L. Tang, X.H. Liang, Mesoporous silica nanoparticles: a promising nanoplatform for treating osteoarthritis and rheumatoid arthritis, ACS Appl. Bio Mater. 9 (6) (2026) 2740–2763.
[35] M. Cedrún-Morales, M. Migliavacca, M. Ceballos, M. Perez-Maseda, G. Zampini, M. T.A. Felgueiras, et al., Clickable polymer-based coatings for modulating the interaction of metal-organic framework nanocrystals with living cells, Acs Appl Mater Inter 17 (17) (2025) 24994–25010.
[36] S. Wu, H. Li, D. Su, N. Lu, Fabrication of docetaxel-loaded hyaluronic acid coated zeolitic imidazolate framework-8 as an effective treatment for leukaemia cancer cells and its apoptosis induction, J. Exp. Nanosci. 19 (1) (2024) 2307061.
[37] J. Yan, C. Liu, Q. Wu, J. Zhou, X. Xu, L. Zhang, et al., Mineralization of pH-sensitive doxorubicin prodrug in ZIF-8 to enable targeted delivery to solid tumors, Anal. Chem. 92 (16) (2020) 11453–11461.
[38] I. Raeisi, Z. Yousefipour, Dual-responsive drug carrier based on zeolitic imidazolate framework-8 incorporated into gold nanoparticles/chitosan/copper sulfide for controlled drug delivery, J. Drug Deliv. Sci. Technol. 98 (2024) 105883.
[39] M. Cai, G. Chen, L. Qin, C. Qu, X. Dong, J. Ni, X. Yin, Metal organic frameworks as drug targeting delivery vehicles in the treatment of cancer, Pharmaceutics 12 (3) (2020) 232.
[40] L. Gong, H. Zhao, L. Chen, Y. Liu, H. Wu, C. Liu, et al., Novel peptide-modified zeolitic imidazolate Framework-8 nanoparticles with pH-Sensitive release of doxorubicin for targeted treatment of colorectal cancer, Pharmaceutics 17 (2) (2025).
[41] N.M. AlSawaftah, N.S. Awad, W.G. Pitt, G.A. Husseini, pH-Responsive nanocarriers in cancer therapy, Polymers 14 (5) (2022).
[42] Y. Yang, Z. Wang, Y. Peng, J. Ding, W. Zhou, A smart pH-Sensitive delivery system for enhanced anticancer efficacy via paclitaxel endosomal escape, Front. Pharmacol. 10 (2019), 2019.

[43] M.J. Jo, H.J. Shin, M.S. Yoon, S.Y. Kim, C.E. Jin, C.-W. Park, et al., Evaluation of pH-Sensitive polymeric micelles using citraconic amide bonds for the Co-Delivery of paclitaxel, etoposide, and rapamycin, Pharmaceutics 15 (1) (2023) 154.
[44] W. Wei, P. Lu, Engineering pH and temperature-triggered drug release with metal-organic frameworks and fatty acids, Molecules 29 (22) (2024) 5291.
[45] A. Maleki, M.A. Shahbazi, V. Alinezhad, H.A. Santos, The progress and prospect of zeolitic imidazolate frameworks in cancer therapy, antibacterial activity, and biomineralization, Adv. Healthcare Mater. 9 (12) (2020) 2000248.
[46] S.A. Polash, A. Poddar, S. Pyreddy, F. Carraro, A.M. D'Angelo, G. Bryant, et al., Phase characterization and bioactivity evaluation of nucleic acid-encapsulated biomimetically mineralized ZIF-8, Acs Appl Mater Inter 17 (2) (2025) 3002–3012.
[47] G.L. Wu, W.Q. Du, B.C. Yu, S. Song, L.H. Gong, L. Wan, Z.L. Li, pH-Triggered tannic acid release from ZIF-8@ZIF-L for intelligent self-healing epoxy coatings in marine environments, Acs Appl Mater Inter 18 (19) (2026) 28054–28068.